ACS OMEGA

Open Access

http://pubs.acs.org/journal/acsodf

Article

A Novel G-Quadruplex Structure within Apolipoprotein E Promoter: A New Promising Target in Cancer and Dementia Fight?

Valentina Pirota,* Angela Dello Stritto, Lisa Rita Magnaghi, Raffaela Biesuz, Filippo Doria, Mariella Mella, Mauro Freccero, and Emmanuele Crespan

Cite This: *ACS Omega* 2024, 9, 45203−45213

Read Online

ACCESS | Metrics & More | Article Recommendations | Supporting Information

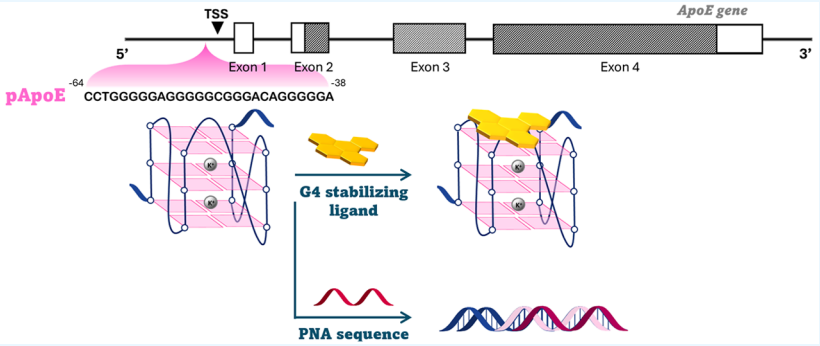

ABSTRACT: Human apolipoprotein E (APOE) is a crucial lipid transport glycoprotein involved in various biological processes, including lipid metabolism, immune response, and neurodegeneration. Elevated APOE levels are linked to poor prognosis in several cancers and increased risk of Alzheimer's disease (AD). Therefore, modulating APOE expression presents a promising therapeutic strategy for both cancer and AD. Considering the pivotal role of G-quadruplex (G4) structures in medicinal chemistry as modulators of gene expression, here, we present a newly discovered G-quadruplex (G4) structure within the ApoE gene promoter. Bioinformatic analysis identified 21 potential G4-forming sequences in the ApoE promoter, with the more proximal to the transcription start site, pApoE, showing the highest G-score. Biophysical studies confirmed the folding of pApoE into a stable parallel G4 under physiological conditions, supported by circular dichroism, NMR spectroscopy, UV-melting, and a quantitative PCR stop assay. Moreover, the ability to modulate pApoE-G4 folding was demonstrated by using G4-stabilizing ligands (HPHAM, Braco19, and PDS), which increased the thermal stability of pApoE-G4. In contrast, peptide nucleic acid conjugates were synthesized to disrupt G4 formation, effectively hybridizing with pApoE sequences, and confirming the potential to unfold G4 structures. Overall, our findings provide a mainstay for future therapeutic approaches targeting ApoE-G4s to regulate APOE expression, offering potential advancements in cancer and AD treatment.

INTRODUCTION

Human apolipoprotein E (APOE) is a 299 amino acid lipid transport glycoprotein encoded by the polymorphic apolipoprotein E gene (ApoE), which is mapped to chromosome 19q13.2.[1] Along with its multifunctional role in lipid transport and metabolism, APOE is involved in the regulation of a spectrum of other biological processes, including DNA synthesis, cell proliferation, differentiation, immune stress, angiogenesis, and metastasis.[2] Interestingly, APOE overexpression has been reported in a wide range of human cancers, like prostate, colorectal, gastric, pancreatic, bladder, ovarian, thyroid, breast, endometrial, and lung cancers, as well as hepatocellular carcinoma, glioblastoma, and lymphoma.[1] Elevated APOE levels correlate with advanced tumor stages, metastases, and poorer prognosis, impacting patients' survival.[1,3] Consequently, targeting APOE expression has yielded countless benefits, including inhibition of cancer cell growth and proliferation, suppression of cell migration, reduction in metastases, induction of cancer cell apoptosis, and increased susceptibility to chemotherapeutic agents.[4,5] Accordingly, effective modulation of ApoE gene expression emerges as an attractive avenue for new therapeutic strategies in cancer management, either as a chemotherapy adjuvant or immunotherapeutic agent.[4−6]

In addition, emerging evidence underscores the crucial role of APOE in modulating processes related to dementia. APOE was found co-deposited with amyloid-β plaques and neuro-

Received: July 11, 2024
Revised: September 27, 2024
Accepted: October 3, 2024
Published: October 30, 2024

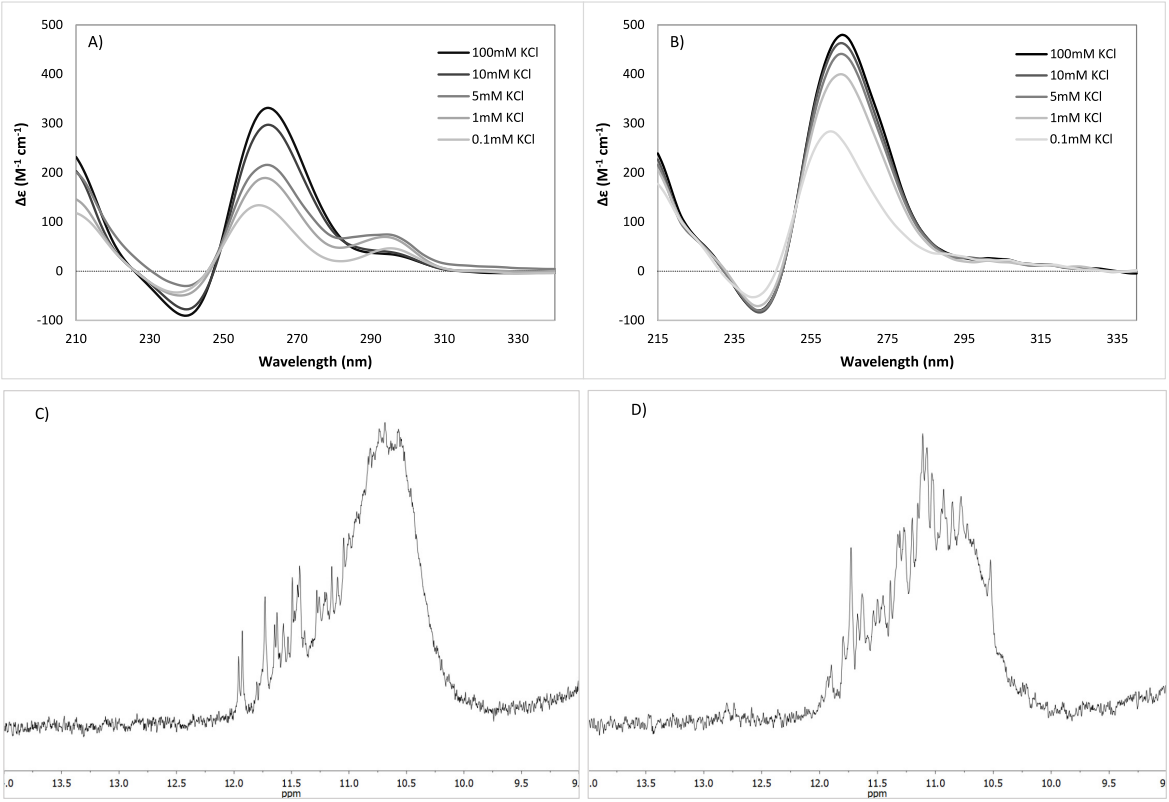

Figure 1. Biophysical demonstration of pApoE-G4s folding. CD spectra of 2.5 μM A) pApoE and B) pApoE$_{ext}$ at different potassium concentrations (from 0.1 to 100 mM) in 10 mM lithium cacodylate buffer, pH 7.2, at 20 °C. ^{1}H NMR spectra of 0.15 mM C) pApoE and D) pApoE$_{ext}$ in 90% H_2O/10% D_2O solution with 100 mM KCl and 20 mM potassium phosphate buffer, pH 7.4, at 25 °C.

fibrillary tangles aggregates in the brain of Alzheimer's disease (AD) patients, and it is intricately involved in distinct functions as regulating lipid transport in the normal and injured central nervous system, glucose metabolism, neuronal signaling, and neuroinflammation.[7−9] In particular, the linkage between the polymorphism in the ApoE gene and the higher genetic risk of developing late-onset AD has been well recognized. However, there is ongoing debate regarding the therapeutic direction for AD, with conflicting findings on the effects of altering APOE levels and also in relation to the specific isoforms. Some studies indirectly suggest that increasing human APOE levels and lipidation may reduce Aβ deposition and restore cognitive function in mouse models of amyloid pathology,[9] while others demonstrated a significant decrease in Aβ-plaques deposition and microglial activation through genetic manipulation of ApoE gene dosage, independent of isoform status.[10,11] Remarkably, data from a rare individual lacking APOE highlighted the complete absence of cognitive deficits, normal brain MRI findings and normal cerebrospinal fluid levels of Aβ and tau proteins.[12] These data emphasize that a decrease in the APOE level, regardless of its isoform, may also result in an effective treatment approach for AD.

Considering these biological insights, we proposed targeting a newly discovered G-quadruplex (G4) nucleic acid structure as an original strategy to modulate ApoE gene expression. G4s are higher-order secondary nucleic acid structures widely distributed across the genome, arising in regulatory regions, rich in guanines, such as promoters, 5′ untranslated regions, transcription factor binding sites, and telomeres.[13−15] Their existence in live cells and pivotal role in influencing different biological processes are strongly supported by experimental data.[16−18] In particular, it is known that the folding modulation of G4s located in the gene promoters interplays with the regulation of transcription processes.[16,19]

Under physiological conditions, four guanines (Gs) can associate through Hoogsteen-type hydrogen bonds to form G-tetrads, square-planar quartets that arrange neatly on top of one another, forming the mainstay of G4 structures, strongly stabilized by cations that fit into the anionic cavities between G-tetrads and coordinated the carbonyl oxygens in position 6. Larger ions, like K^+, strongly stabilize G4 structures by binding in the interplane cavity, while smaller ions, such as Li^+, are too small to effectively fit in the cavity and contribute little to G4 formation/stabilization.[20,21] Considering this unique structure of discrete folded globular DNAs, which sets them apart from other nucleic acid structures, G4s targeting with small molecules has proven to be a profitable strategy similar to drug targeting of folded proteins.[22]

Therefore, in this work, we proposed the targeting of newly discovered DNA-G4 (pApoE), located upstream of the transcription start site of the ApoE gene, as an innovative and promising strategy to effectively regulate ApoE expression. After proving the ability of this nucleobase sequence to fold into a very stable parallel G4 via biophysical studies, the use of well-known G4 stabilizing ligands (HPHAM,[23] Braco19,[24] and PDS)[25] confirmed pApoE-G4 stabilization under physiological conditions. Likewise, three distinct short peptide nucleic acid (PNA) conjugates, synthesized for hybridizing with a portion of the G4 nucleobases sequence, were used to corroborate the possibility of pApoE-G4 unfolding.[26] Testing both stabilizing and disrupting G4-ligands is based on the understanding that,

https://doi.org/10.1021/acsomega.4c06430
ACS Omega 2024, 9, 45203−45213

Table 1. G-Score Values Comparison between pApoE and Other Well-Known G4 Structures

Name	Base sequences (5′−3′)	QGRS Mapper G-score	G4Hunter score
pApoE	**$G_5AG_5CG_3ACAG_3$**	**42**	**2.67**
c-Myc	$TG_4AG_2TG_4AG_3TG_4A_2G_2$	41	2.59
VEGF	$G_3AG_3T_2G_4TG_3$	41	2.53
Bcl-2	$G_3CG_3CGCG_3AG_2A_2G_5CG_3$	40	2.11
KRAS	$AG_3CG_2TGTG_3A_2GAG_3A_2GAG_5AG_2$	40	1.78
CKIT-1	$AG_3AG_3CGCTG_3AG_2AG_3$	39	1.77
22AG	$AG_3T_2AG_3T_2AG_3T_2AG_3$	42	1.64
CKIT-2	$C_3G_3CG_3CGCGAG_3AG_4AG_2$	38	1.42
HRAS-1	$TCG_3T_2GCG_2CGCAG_2CACG_3CG$	41	1.19

in the context of gene promoters, some G4 structures can act as transcriptional repressors, while others may function as enhancers.[27,28]

ApoE-G4 targeting for modulating ApoE expression is a high-impact challenge that has never been attempted before. In this sense, our preliminary results are mainstays for a future understanding of how the variation in ApoE levels is related to the onset and evolution of cancer disease as well as dementia, paving the way for the development of innovative therapeutic strategies.

RESULTS AND DISCUSSION

G-Quadruplex Prediction by Bioinformatic Studies and Its Promising Location on ApoE Promoter Region. The promoter region of ApoE (GRCh38: 19:44904303:44907502) exhibits a high abundance of G-bases, clustered in groups of 2−5 continuous G, contributing to an overall GC% of 57.31% (Figure S1).

Through a preliminary bioinformatic evaluation ("QGRS Mapper",[29] and "G4 Hunter"),[30] we have been able to endorse twenty-one putative quadruplexes (PQs) within this region, excluding overlaps (Table S1), where the likelihood to form a stable G4 is evaluated by a G-score ranking. Notably, among the identified PQs, pApoE (5′-$G_5AG_5CG_3ACAG_3$-3′) exhibits the highest G-scores and is located proximal to the main transcription starting site (TSS), spanning from −61 to −41. Moreover, the calculated pApoE G-score compares favorably with those of well-known G4 structures (Table 1),[31] resulting in slightly higher than c-Myc, the most stable G4 known.

Its predicted G4 stability and its location close to TSS (−61/−41) outline the pApoE potential as a highly interesting region to target ApoE expression. Indeed, the ApoE proximal promoter contains a GC box transcriptional control element at −59/−45 bases range, which is the binding site for the Sp1 transcription factor.[32] Sp1 interacts with a positive element for transcription within URE1 regions (−161/−141), which acts as an enhancer element, suggesting that this complex can play an important role in the basal level of ApoE expression. The region from −74 to −48 was identified as recombinant AP2 binding sites and the ones from −65 to −54 as Zinc1 and Zinc2 transcription factors binding sites.[32,33] Moreover, tumor progression locus 2 and mitogen-activated protein kinase/ERK kinase kinase 1 signaling pathways converge to nuclear factor kappa-light-chain-enhancer of activated B cells and activator protein 1, acting on the ApoE core promoter in the −55/+73 range. They are extremely important because they are recognized as primarily responsible for the downregulation of ApoE promoter activity by lipopolysaccharide.[32,34]

Biophysical Confirmation of the Existence of a G4 Structure on the ApoE Promoter and Evaluation of Their Stability. To assess the propensity of pApoE sequence 5′-$G_5AG_5CG_3ACAG_3$-3′ in folding into a stable G4, circular dichroism (CD) spectra of a model oligonucleotide (2.5 μM) were recorded at different potassium concentrations (100, 10, 5, 1, and 0.1 mM) in 10 mM lithium cacodylate buffer pH 7.2 at 20 °C (Figure 1A). LiCl was added in the proper quantities to keep the ionic strength at 100 mM. Under much more similar to physiological conditions (100 mM KCl), the sequence folded into a parallel topology (calculated to be 99.0%;Figure S2A),[35] as evidenced by a positive band at 262 nm, a negative one at 240 nm, and a positive one at around 210 nm (a feature which differentiates it from an A-form of DNA).[36,37] A quantitative analysis of secondary structure estimated the presence of 51.05%*anti-anti* and 1.00%*syn-anti* glycosidic bond conformations, with 25.60% of diagonal and lateral loops and 22.35% of other conformations (Figure S2B).[35] At lower potassium concentrations (0.1 mM), the sequence underwent rearrangement, resulting in a mixture of two G4 topologies at the equilibrium: 58.9% parallel and 41.1% antiparallel, characterized by the increase of the peak at 295 nm (Figures 1A and S2A).[35] Indeed, G4 antiparallel topology is characterized by a positive band at around 295 nm and a negative one at 260 nm.[37]

To explore the influence of neighboring nucleobases on the folding of the pApoE structure, an extended sequence, $pApoE_{ext}$ 5′-$C_2TG_5AG_5CG_3ACAG_5A$-3′, was analyzed. $pApoE_{ext}$ includes the three nucleobases CCT and GGA which, respectively, precede and follow the sequence of pApoE in the genome. Despite the introduction of six nucleobases, including two additional guanines, the original parallel topology is retained (Figure 1B) even at low KCl (0.1 mM) concentrations. Estimated fractions of the tertiary elements correspond to 100% parallel topology with 100 mM KCl that decreases at 96.67% in the presence of 0.1 mM KCl (with a 3.33% antiparallel component) (Figure S2C). In this case, the *anti-anti* glycosidic bond conformation is predominant at all analyzed potassium concentrations resulting equal to 73.23% with 100 mM KCl (Figure S2D).[35] The Supporting Information includes a summary of the evaluated secondary and tertiary structure fractions of pApoE and $pApoE_{ext}$ as a function of KCl concentrations (Figure S2).

In addition, the folding of pApoE-G4s was corroborated by the ^{1}H-NMR signals within the range of 10.5−12 ppm, characteristic of Gs imino protons when a G-tetrad is formed (Figure 1C,D).[38]

CD melting experiments (20−95 °C) in 10 mM lithium cacodylate buffer at pH 7.2, revealed the exceptional stability of both pApoE G4 structures. The melting temperatures (T_m) for pApoE were 58.2 ± 0.3 °C with 5 mM KCl and 44.0 ± 0.2 °C with 0.1 mM KCl. Conversely, in the case of $pApoE_{ext}$ T_m at

https://doi.org/10.1021/acsomega.4c06430
ACS Omega 2024, 9, 45203−45213

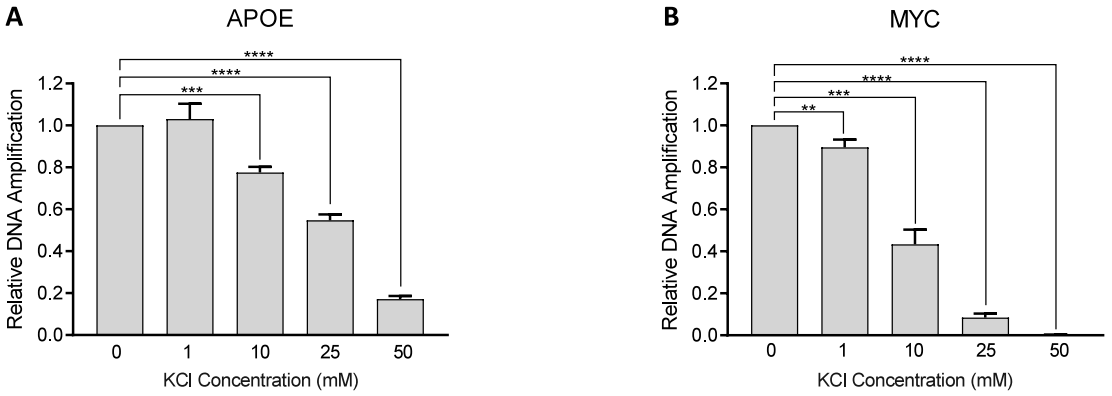

Figure 2. qPCR Stop Assay performed with variable concentration of KCl. KCl-mediated stabilization of A) APOE and B) MYC G-quadruplexes hampered DNA amplification. In each qPCR reaction, the Ct values of ApoE and MYC G4-sequences were compared to the Ct values of the Actin No-G4 sequence. Error bars represent the mean and DS of three independent experiments. Two-tailed unpaired Student's t test was used to calculate p-values. *P < 0.05, **P < 0.01, ***P < 0.001, ****P < 0.0001.

0.1 mM was 51.1 ± 0.4 °C, while at higher concentrations T_m values exceeded the experimental range (>95 °C).

To evaluate pApoE-G4s stability related to other well-known parallel G4s, we tested five model oligonucleotides (Myc-23456, cMyc, Bcl-2, CKIT-2, and CKIT-1)[31,39] using different KCl concentrations to maintain T_m values within the 50−60 °C range. pApoE showed stability comparable to that of the model sequence Myc-23456, the most stable parallel G4 known, with equivalent T_m values observed at 5 mM KCl (Table S2). $pApoE_{ext}$ demonstrated significantly higher stability than the tested model oligonucleotides, melting at around 50 °C with only 0.1 mM KCl, a concentration 50 times lower than that required for the Myc-23456 and cMyc models (Table S2).

pApoE-G4s high stability of pApoE-G4s was further confirmed by UV-melting experiments, following the decrease of the absorbance at 295 nm as a function of temperature increase (20−95 °C). Midtransition temperatures ($T_{1/2}$) correspond to the ones obtained by CD-melting and were equal to 43.0 ± 0.4 °C and 54.0 ± 0.3 °C for pApoE and $pApoE_{ext}$ respectively in 10 mM lithium cacodylate buffer at pH 7.2, with 0.1 mM KCl and 99.9 mM LiCl (Table S3). In addition, an estimation of model-dependent thermodynamic parameters was gained from these UV-melting curves. Van 't Hoff enthalpy and entropy values correspond to −39 ± 1 kcal mol^{-1} and −121 ± 3 cal mol^{-1} K^{-1} for pApoE, and to −44.3 ± 0.8 kcal mol^{-1} and −139 ± 4 cal mol^{-1} K^{-1} for $pApoE_{ext}$ (Table S3).[40]

UV−vis thermal difference spectra (TDS), obtained by the subtraction of the spectra of unfolded (temperature above T_m) and folded (low temperature) G4s, were exploited to further confirm the folding of these two sequences into G4s. The presence of a negative peak at 295 nm, and positive ones at 273, 253, and 245 nm correspond to the feature bands of TDS-G4s (Figure S3).[41]

To confirm the G4 structure formation on the sequences of interest, a quantitative PCR stop assay (qPCR) was carried out on genomic DNA extracted from SK-MEL-30 cells. This assay ensured the folding of pApoE sequences into G4 structures even within human genomic DNA.[42] Quantitative amplification was performed on both the ApoE promoter (Figure 2A) and the MYC promoter, which served as positive controls for G4 formation (Figure 2B). The actin No-G4 sequence was used as a negative control. The presence and subsequent stabilization of G4s on genomic DNA hindered the amplification process in a KCl concentration-dependent manner.

Effectiveness of Small Molecules' Manipulation of pApoE-G4s Folding. The possibility of stabilizing the pApoE-G4s folding was verified using three well-recognized, highly powerful G4-ligands (G4Ls): HPHAM, a core-extended naphthalene diimide designed and synthesized by some of us,[23] Pyridostatin (PDS), a bisquinoline-2,6-dicarboxamide derivative,[25] and Braco19, an acridine derivative[24] (Figure S4). All three G4Ls significantly perturbed the original structures of both pApoE-G4s, leading to partial reorganization of their G4-topologies. This was evident from the evaluation of the tertiary structures obtained through CD spectra processing, which were recorded in the presence of 2.5 μM pApoE-G4s, 4 equiv of G4Ls, 100 mM of KCl, and 10 mM of lithium cacodylate buffer at pH 7.2 (Figure S5). Specifically, G4Ls interaction with the target decreased the parallel component from 99.0% to roughly 70% in the case of pApoE, and from 100% to approximately 50% in the case of $pApoE_{ext}$.

Nevertheless, CD- and FRET-melting experiments highlighted that all three ligands effectively stabilized both pApoE-G4s by at least 15 °C (Table 2). Despite the low potassium concentrations required for these assays (more than 3 orders of magnitude lower than the physiological cell concentrations), the best-performing ligand, PDS, exhibited a substantial thermal stabilization effect on both pApoE-G4s, preventing the calculation of melting temperature values within 95 °C.

Table 2. Variations of the Melting Temperatures (ΔT_m) and Mid-Transition Temperatures ($\Delta T_{1/2}$) Obtained from the Interaction between pApoE-G4s and G4Ls[a]

	ΔT_m (°C) by CD-melting		$\Delta T_{1/2}$ (°C) by FRET-melting	
G4 Ligands	pApoE	$pApoE_{ext}$	pApoE	$pApoE_{ext}$
HPHAM	28.0 ± 0.9	37.4 ± 0.7	29.3 ± 0.9	38 ± 1
PDS	>51.0	>43.9	>47.5	>53.4
BRACO19	15.3 ± 0.7	14.5 ± 0.5	16 ± 1	15.0 ± 0.7

[a]2.5 μM or 0.25 μM, for CD- and FRET-melting experiments respectively, of pApoE or $pApoE_{ext}$ in the presence of 4 equiv of G4-ligands, 0.1 mM KCl, 99.9 mM LiCl, and 10 mM lithium cacodylate buffer pH 7.2.

https://doi.org/10.1021/acsomega.4c06430
ACS Omega 2024, 9, 45203−45213

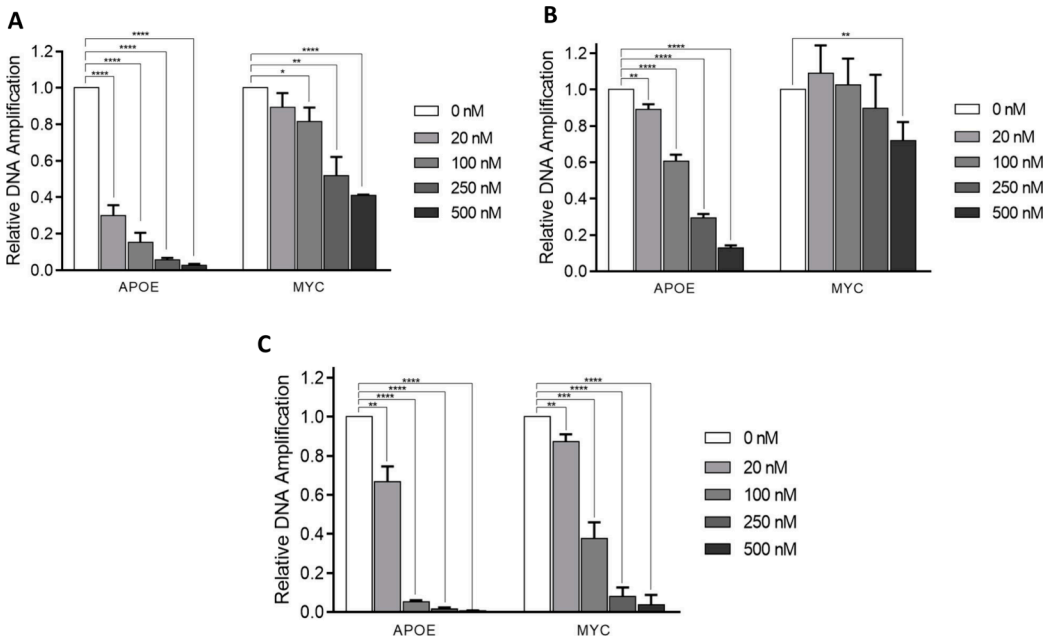

Figure 3. qPCR Stop Assay in the presence of G4-stabilizing agents. The quantitative PCR was clearly altered by the presence of HPHAM (3A), Braco-19 (3B), and PDS (3C). The reaction is normalized on ACTN, a non-G4 sequence. Error bars represent the mean and DS of three independent experiments. Two-tailed unpaired Student's *t* test was used to calculate *p*-values. *$P < 0.05$, **$P < 0.01$, ***$P < 0.001$, ****$P < 0.0001$.

Additionally, as HPHAM, Braco-19, and PDS are unspecific G4 ligands, we compare their effect on MYC and ApoE by the qPCR stop assay. All G4 ligands affect the amplification on both sequences in a dose-dependent manner, with HPHAM and PDS exhibiting higher activities (compare Figure 3A,C with Figure 3B). Importantly, all reactions were performed with 10 mM KCl, a condition in which we observed a reduction of about 50% in ApoE and 20% in Myc G4. Nonetheless, all ligands clearly show a stronger amplification inhibition toward APOE than toward the MYC sequence.

In the attempt to specifically unfold pApoE-G4 sequences, two different short peptide nucleic acids (PNAs) were designed and tailored to hybridize with specific segments of pApoE-G4s nucleobases, thereby forcing the unfolding of G4 structure through the formation of PNA-DNA duplexes/triplexes.[26,43] Specifically, PNA-1 was engineered to hybridize with the initial seven G-bases, spanning from G_4 to G_{11}, while PNA-2 was synthesized to pair with the seven guanines ranging from G_{10} to G_{17} (Table S4). To enhance the PNAs solubility and facilitate potential future delivery to the ApoE promoter, the nuclear localization sequence H_2N-ProLysLysLysArgLysVal-OH[44] was conjugated to the PNAs C-terminus, along with the addition of a glycine residue as a spacer. Their efficacy in disrupting the previously folded pApoE-G4 sequences in the presence of 100 mM KCl in 10 mM lithium cacodylate buffer (pH 7.2) was evaluated by CD analysis. The addition of 1 equiv of either PNA-1 or PNA-2 reveals a reduction in intensity and a red-shift of both pApoE-G4s dichroic signals, with positive bands, observed around 270−275 nm and negative ones around 245−250 nm (Figure 4A). These spectral changes provided compelling evidence of PNA-DNA duplex formation, indicative of pApoE-G4s unfolding. Additionally, the formation of B-form structures was validated by evaluating these CD spectra through the XGBoost algorithm prediction method (accuracy 87.33%).[45]

Fascinating, PNA-1 and PNA-2 conjugates are also able to interfere with HPHAM in pApoE-G4 binging. Indeed, the addition of 10 μM of PNA conjugates at a pre-stabilized pApoE (2.5 μM) G-quadruplex with 4 equiv of HPHAM (10 μM) induced a red-shift of the dichroic signal of 5 nm consistent with a binding competition (Figure 4C). Considering the potential utility of an emitting species to track the behavior of our PNA conjugates within cells in future studies, we decided to conjugate a Coumarin 343 residue to the N-terminus of PNA-2, which demonstrated superior disrupting performances on both pApoE-G4 sequences (Table S4). To further enhance PNA-DNA hybridization, an additional cytosine residue tailored to hybridize with G_{18} was added, and the dye was spaced through a lysine residue, which, being positively charged, boosts the electrostatic interaction between the two strands. CD spectra confirmed that the steric hindrance of Coumarin did not interfere with the ability of our conjugate in pApoE-G4s disruption, highlighting PNA-Cum as the best candidate in terms of biophysical performance (Figure 4). The melting temperature of this newly formed heteroduplex was determined to be 48.5 ± 0.4 °C, underscoring a robust and stable interaction even at physiological temperature (37 °C). This observation highlights the potential utility and resilience of the interaction under conditions relevant to biological systems.

The interaction of HPHAM or PNA-Cum with the $pApoE_{ext}$ oligonucleotide was further analyzed using ^{1}H-NMR spectroscopy at a 1:1 molar ratio (0.15 mM). The addition of 1 equiv of HPHAM prompted a reorganization of the G4 structure, as indicated by the changes in the imino proton signals between 10.5 and 12 ppm, corresponding to the G4 structures (Figure S6A).[38] Despite the different working concentrations, this result aligns with the CD spectra (Figure S5C), which suggested a structural shift toward a hybrid topology (Figure S5D). Conversely, the addition of one equivalent of PNA-Cum left the G4 region signals largely unchanged, although a broad,

https://doi.org/10.1021/acsomega.4c06430
ACS Omega 2024, 9, 45203−45213

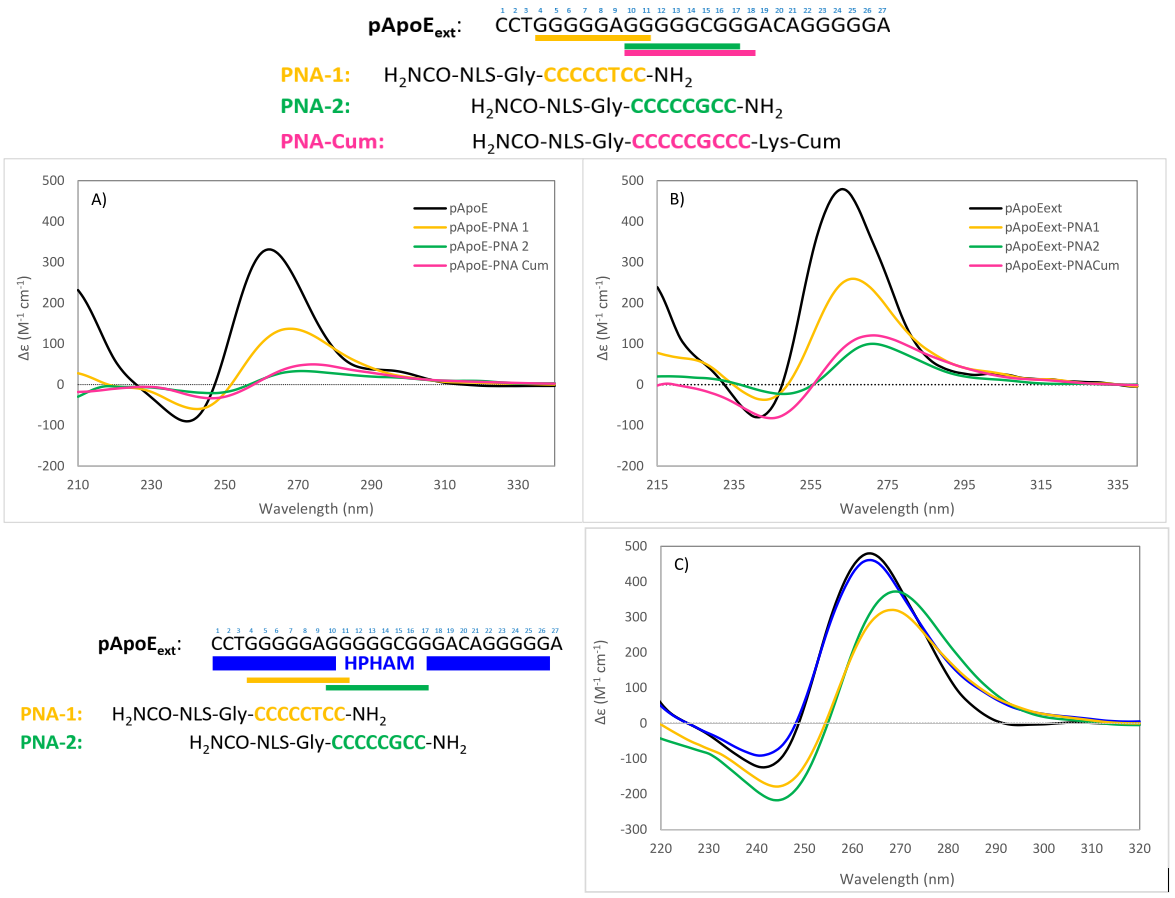

Figure 4. CD spectra of 2.5 μM pApoE (A) and pApoE$_{ext}$ (B) in the presence of 2.5 μM PNA conjugates, in 100 mM KCl, and 10 mM lithium cacodylate buffer, pH 7.2, 25 °C. C) CD spectra of 2.5 μM pApoE$_{ext}$ (black) in the presence of 10 μM HPHAM (blue) and after the addition of 10 μM PNA-1 (yellow) or PNA-2 (green) in 0.1 mM KCl, 99.9 mM LiCl and 10 mM lithium cacodylate buffer pH 7.2. Above it is reported a schematic representation of synthesized PNA conjugates. Under are reported the nucleobases involved in the interaction with HPHAM or PNA-1 and PNA-2.

weak signal appeared between 12.0 and 13.2 ppm, attributable to imino protons of guanine bases not involved in an ordered G4 structure (Figure S6B).[46]

Unfortunately, in both experiments, a significant amount of precipitate formed within 30 min of the pApoE$_{ext}$-ligands interaction at room temperature. The solutions were centrifuged, the aqueous supernatants were removed, and the precipitate was dissolved in DMSO. Then, both phases were diluted in 10 mM lithium cacodylate buffer (pH 7.2), and CD spectra were recorded. In the case of HPHAM addition, the CD spectra from both DMSO and aqueous phases were nearly identical (Figure S7A). However, for PNA-Cum, the aqueous phase resembled the dichroic signal of pApoE$_{ext}$, while the precipitate showed characteristics more consistent with the PNA:DNA double-strand interaction (Figure S7B).

To better appreciate how G4-stabilizing ligands (HPHAM, PDS, and Braco19) as well as PNA conjugates (PNA-1, PNA-2, PNA-Cum) affected the original pApoE topologies, CD spectra recorded in the presence of both the two interacting tools (Figures S5 and S4) were analyzed by applying different chemometric analysis. Principal Component Analysis on centered CD spectra was first used to visualize G4 topologies (*unsupervised analysis*). It was run on the reference data set, and the first two components, PC1 and PC2, turned out to be significant in distinguishing the samples' topologies. More specifically, the loading plots display that G4s topologies are separated alongside PC1 (Explained Variance 89.57%) according to their ellipticity in the region around 264 nm while distinction on PC2 (E.V. 7.99%) based on samples behavior around 290 nm (Figure S8). This result is congruent with the representative CD peaks of parallel, antiparallel, and hybrid G4s topologies.[37]

The score plot perfectly summarizes the differences in G4 topologies: separation between parallel and antiparallel structures is the main phenomenon, described by PC1 and accounting for almost 90% of the overall experimental variance, while recognition of hybrid structures alongside PC2 represents a minor effect (Figure S9A). By projecting our samples on the score plot, it was evident that the CD spectra of pApoE wild-type, as well as of pApoE in the presence of HPHAM (pApoE-HPHAM), PDS (pApoE-PDS), and Braco19 (pApoE-Braco19) were undoubtedly superimposed on parallel G4 structures, unlike pApoE-PNAs interacting systems (Figure S9B). To develop a mathematical model for verifying the compatibility of the test samples with the topologies of interest, we moved to a *supervised analysis* exploiting a class-modeling approach.[47]

In light of the meaningful results obtained from PCA analysis, the class-modeling approach was performed by applying SIMCA[47,48] to model parallel, hybrid, and antiparallel classes. The reference data set was exploited to train the models to recognize the distinctive features of G4 topologies of

https://doi.org/10.1021/acsomega.4c06430
ACS Omega 2024, 9, 45203−45213

interest (performances for models built on the three classes are reported in Table S5). Consistent with the estimated fractions of tertiary elements (Figure S5B) and PCA, pApoE, pApoE-HPHAM, pApoE-PDS, and pApoE-Braco19, were classified as primarily parallel G4 structures (Figure S10). Otherwise, pApoE-PNAs interacting systems were excluded from all three analyzed classes, apart from pApoE-PNA-2 whose CD spectrum resulted in slightly compatible with antiparallel G4 topology (Figure S10).

CONCLUSION

In this study, we identified a new G4 structure within the promoter region of the ApoE gene, named pApoE, as a potential target for reaching effective modulation of ApoE expression. Bioinformatic analyses revealed that this novel sequence has a higher G-score compared to that of well-known G4 structures, suggesting its significant stability and potential functional relevance. Additionally, the location of pApoE within the binding site for different transcription factors emphasized its potential importance. The propensity of pApoE, as well as $pApoE_{ext}$ (an extended sequence of pApoE), to fold into highly stable parallel G4 under physiological conditions was confirmed by CD, NMR, and UV-melting studies. Both sequences exhibited melting temperatures exceeding 95 °C in the presence of 100 mM KCl. Additionally, quantitative PCR stop assays further validated the formation of pApoE-G4s within the genomic DNA of SK-MEL-30 cells, indicating their presence and stability in a cellular context. The effectiveness in modulating pApoE-G4s folding was demonstrated through interaction with small molecules. Three well-known G4 ligands (HPHAM, PDS, and Braco19) were tested for their stabilizing effects. PDS showed the most substantial CD-melting effect, increasing the melting temperature by over 50 °C, while HPHAM drastically impaired genomic DNA amplification already at 20 nM concentration. In contrast, peptide nucleic acid conjugates were engineered to successfully disrupt pApoE-G4 structures by hybridization with specific segments of the G4 sequence. Notably, a coumarin-labeled PNA (PNA-Cum) demonstrated superior performance in unfolding the G4 structures, maintaining a stable interaction at physiological temperatures (T_m = 48.5 ± 0.4 °C). In conclusion, the successful demonstration of pApoE-G4s' stability and their modulation by small molecules and PNA-conjugates provides a promising strategy for the future modulation of ApoE expression in vitro and in vivo.

EXPERIMENTAL SECTION

Materials. Solvents, salts, and reactants were purchased from Zentek (Milan, Italy) and used as they were without purification. Model oligonucleotides for biophysical studies were purchased from Biomers.net (Ulm, Germany) with an HPLC grade of purification. PNA monomers were bought by Panagene (Daejeon, South Korea), and Fmoc-protected amino acids and resins were from Novabiochem (Merck, Milan, Italy). Braco19 is commercially available and was purchased from Merck (Darmstadt, Germany) as hydrochloride salts. HPHAM[49] and PDS[50] were synthesized following the protocols previously reported in the literature, confirming their correspondence by ^{1}H-NMR and mass spectrometry. Their purity grades were checked by analytic HPLC (Agilent system SERIES 1260, Agilent Technologies, Santa Clara, CA, USA), confirming to be >98% (Figures S11 and S12). Column: XSelect HSS C18 (2.5 μm, 4.6 × 50 mm); flow rate: 1.4 mL/min; method: isocratic gradient over 2 min 95% of H_2O + 0.1% trifluoroacetic acid (5% acetonitrile), gradually to 40% aqueous solvent over 6 min; λ = 210 nm, 256 nm.

Bioinformatics Studies. The promoter sequence analyzed corresponds to the region on Chr 19 that involves the nucleobases: from 44904303 to 44907502 (Source: ENSG00000130203). Putative quadruplexes have been identified by the QGRS Mapper software program[29] considering the following restrictions: maximum length of QGRS sequence of 30 nucleotides (nt); minimum number of G-tetrads in a G4 of 2; loops lengths in the range of 0−20 nt; QGRS G-Score value > 15. G4Hunter Score values were evaluated considering a threshold of 1.5 with a window size of 20 nt.[30]

CD Studies. Circular dichroism spectra were recorded using a J-1500 Spectropolarimeter (Jasco Corp., Easton, MD, USA), equipped with a Peltier temperature controller set at 20 °C (Holder control), in a quartz cuvette with 1 cm path length. The oligonucleotide model sequences used here were reported in Table S6.

They were diluted from stock solutions to a final concentration of 2.5 μM in 10 mM lithium cacodylate buffer, pH 7.2, containing different concentrations of KCl (100, 10, 5, 1, and 0.1 mM). Ionic strength was equilibrated at 100 mM by adding proper amounts of LiCl. The solutions were annealed by heating at 95 °C for 5 min and gradually cooling to room temperature over 4 h. G4 ligands were added to folded G4s in 10 μM concentration (4 equiv) and left to equilibrate for 4 h at room temperature before recording CD experiments.

CD spectra were recorded from 210 to 340 nm with a scan speed of 200 nm/min, with a response of 2 s and 1 nm of bandwidth. The reported spectra correspond to the average of 4 scans and were baseline corrected for the signal contribution due to buffer mixture and chloride salts. CD signals were expressed as $\Delta\varepsilon$ (M^{-1} cm^{-1}) in the function of wavelength, according to the relationship $\Delta\varepsilon = \vartheta/(32980 \times C \times l)$, where ϑ corresponded to observed ellipticities (in millidegrees), C is DNA molar concentration, and l is the path length in centimeters (1 cm).

Secondary and tertiary structure fractions predictions were calculated by exploiting the algorithm developed by Del Villar-Guerra et al.[35]

For the CD-melting experiments, the oligonucleotides were annealed as before, diluting their stock solution to 2.5 μM final concentration into a 10 mM lithium cacodylate buffer, pH 7.2, in the presence of 0.01, 0.1, 1, and 5 mM KCl and proper amounts of LiCl. The ellipticity variation was registered at 262 and 292 nm every 0.5 °C, with a temperature scan rate of 1 °C/min from 20 to 95 °C, after a pre-equilibrium of the solution at 20 °C for 5 min. The calculated melting temperature values correspond to the average of two independent experiments, identified according to the Van 't Hoff equation applied for a two-state transition from a folded to an unfolded G4 state. It was assumed that the heat capacity of the folded and unfolded states is equal. ΔT_m values were calculated as the difference T_m in the presence and absence of the compounds.

NMR Studies. ^{1}H-NMR spectra were run on a Bruker Avance NEO 700 MHz (BRUKER, Billerica, MA, USA), endowed with a triple resonance helium-cooled cryoprobe 5 mm. Oligonucleotides (0.15 mM) were dissolved in a 9:1 H_2O:D_2O mixture with 100 mM KCl and 20 mM potassium

https://doi.org/10.1021/acsomega.4c06430
ACS Omega 2024, 9, 45203−45213

phosphate buffer at pH 7.4. The solutions were annealed at 95 °C for 3 min and frozen in ice for 30 min. Subsequently, one equivalent of HPHAM or PNA-Cum was added to the $pApoE_{ext}$ solution, and ^{1}H-NMR spectra were recorded after 4h interaction. ^{1}H-NMR spectra were recorded at 25 °C for 3 h, using zgesgp sequence for water signal suppression. The signals were processed using an exponential apodization along t1 of 3 Hz.

UV Studies. UV spectra were registered using an Agilent Cary 60 spectrophotometer (Agilent Technologies, Santa Clara, CA, USA) equipped with a Single-Cell Peltier temperature controller in a cuvette with 1 cm of path length.

The oligonucleotides were diluted from stock solutions to a final concentration of 2.5 μM in 10 mM lithium cacodylate buffer, pH 7.2, with 0.1 mM KCl and 99.9 mM LiCl (1 and 5 mM KCl were used only for pApoE). The solutions were annealed at 95 °C for 5 min and slowly cooled to room temperature over 4 h before recording UV melting experiments.

UV spectra were recorded from 210 to 340 nm with a scan rate of 50 nm/min, and a slit width of 0.5 nm, in the function of the temperature variation of 1 °C/min from 20 to 95 °C. Data correspond to the average of two independent experiments. All UV data were processed following a reported protocol.[40] Midtransition temperatures were calculated by normalizing the absorbance decreasing at 295 nm versus temperature and identifying the folded fraction of 0.5. Association constants (K_a) were estimated according to the equation $K_a = \alpha_T/(1 - \alpha_T)$, where α_T are the folded fractions. Van 't Hoff enthalpy and entropy values were calculated by restricting the temperature range for which the folded fraction is $0.15 < \alpha < 0.85$, in compliance with the equation $\text{Log } K_a = (-\Delta H°/R) \times ((1/T) + \Delta S°/R)$. UV thermal difference spectra (TDS) have been obtained by the mathematical subtraction of the spectra of fully unfolded oligonucleotides (above T_m, 95 °C) and the spectra of fully folded oligonucleotides (low T, 20 °C).[40]

Cell Cultures. Melanoma-derived human cell line SK-MEL-30[51] was cultured in Roswell Park Memorial Institute (RPMI) 1640 Medium (Euroclone) containing 10% fetal bovine serum (FBS, ThermoFisher), 2 mM L-glutamine, and penicillin-streptomycin, grown at 37 °C and 5% CO_2.

qPCR Stop Assay. Genomic DNA from the SK-MEL-30 cell line was isolated by collecting samples and processing with the NucleoSpin Tissue, Mini kit for DNA from cells and tissue (Macherey-Nagel) according to the manufacturer's instructions. For each reaction, 100 ng of genomic DNA was employed, followed by the addition of 0.5 μM primers, 0.5% (v/v) DMSO (Sigma-Aldrich, Italy), different concentrations of KCl (1, 10, 25, and 50 mM), and iQ SYBR Green Supermix (BioRad, Italy). Therefore, for the qPCR assay with G4-stabilizing compounds, HPHAM, Braco-19, and PDS were employed at different concentrations (500, 250, 100, 20, and 5 nM) with 10 mM KCl. The experiments were performed with a LightCycler 480 System. The amplification process was set up as follows: 95 °C for 5 min, then a three-step reaction of 95 °C for 1 min, 60 °C for 30 s, and 72 °C for 30 s. The C_t values were quantified, and the relative quantification ($\Delta\Delta C_q$ values). The statistical analysis was made using GraphPad Prism, version 7. The primers used for the amplification step are signed in Table S7.

FRET-Melting. Förster Resonance Energy Transfer (FRET)-melting assays were performed using an Agilent AriaMx Real-Time PCR System (Agilent Technologies, Santa Clara, CA, USA) on 96-well plates.

5′-FAM (6-carboxyfluorescein) and 3′-TAMRA (6-carboxy-tetramethylrhodamine) labeled pApoE or $pApoE_{ext}$ model oligonucleotides were diluted from stock solutions to 0.25 μM in 10 mM lithium cacodylate buffer pH 7.2 with 0.1 mM KCl and 99.9 mM LiCl. The mixtures were annealed at 95 °C for 3 min and subsequently frozen in ice for 30 min. G4-ligands were added in 1 μM concentration (4 equiv) and left to equilibrate for 4 h at room temperature. The solutions were equilibrated at 25 °C for 5 min; subsequently, the fluorescent emission at 516 nm (excitation at 462 nm) was measured at each 5 °C following a stepwise increase of 1 °C/min from 25 to 95 °C. Reported data are the average of two independent experiments, each conducted in triplicate. The fluorescence emission increase was reported in the function of the temperature and the sigmoidal curves were normalized, identifying as $T_{1/2}$ the temperature at which fluorescence is 0.5. $\Delta T_{1/2}$ values were calculated as the difference between $T_{1/2}$ values in the presence and absence of G4 ligands.

Synthesis of PNA Conjugates. PNAs conjugates were assembled by stepwise microwave-assisted Fmoc-SPPS on a semiautomatic synthesizer (Biotage Initiator+), operating in a 0.04 mmol scale on a Rink Amide resin (100−200 mesh; loading 0.37 mmol/g). The resin was preswelled for 1 h in DCM and 1 h in DMF and submitted to the preliminary Fmoc-deprotection step, using 25% (v/v) piperidine in DMF.

The amino acid coupling reactions were performed using 3 equiv of Fmoc-protected amino acids in the presence of 3 equiv of HOBt, 3 equiv of PyBOP, and 6 equiv of DIPEA in 1:1 DMF and DCM mixture. Coupling steps were performed for 15 min at 50 °C.

For assembling PNA monomers, the coupling reactions were performed using 3 equiv of monomers in the presence of 3.5 equiv of Oxyma Pure, and 3.5 equiv of *N*,*N*′-diisopropylcarbodiimide in 1:1 NMP and DCM mixture. Coupling steps were carried out for 35 min at 75 °C. All the deprotection steps were done by treating the resin twice with a 25% piperidine solution in DMF at room temperature.

Coumarine 343 was synthesized following an already published protocol and its identity and purity were assessed by analytic HPLC and ^{1}H-NMR.[52] The dye (5 equiv) was directly conjugated to the peptide-PNA sequence on the solid support using 5 equiv of HATU and 10 equiv of DIPEA, by vortexing the mixture for 2 h at room temperature. PNA conjugates were cleaved from the resin using a TFA:TIS:Milli-Q H_2O (95:2.5:2.5, v/v) solution. After stirring at room temperature for 3 h, the resin was removed by filtration under reduced pressure, and cold diethyl ether was added to induce the PNA-conjugates precipitation.

The crudes were filtered and washed with cold diethyl ether, resuspended in acidic water (0.1% TFA), and purified by preparative HPLC (Agilent Technologies 1260 Infinity HPLC) equipped with a diode array detector. A Waters XSelectHSS C18 (2.5 μm, 50 mm × 4.6 mm) column was used combining acidic water (0.1% TFA) and acetonitrile as eluents. Purification method: 2 min 95% acidic water, followed by a 14 min gradient step reaching 60% aqueous phase; flow rate of 30 mL/min; λ = 210, 256 nm. The purity of PNA conjugates was evaluated by analytic HPLC, resulting >97.5% (Figures S13−S15).

PNA conjugates were characterized by using a surveyor UHPLC system (Thermo Finnigan, San Jose, CA, USA)

https://doi.org/10.1021/acsomega.4c06430
ACS Omega 2024, 9, 45203−45213

equipped with a BEH Acquity UPLC column (1.7 μm) 2.1 mm × 50 mm, and an LCQ ADV MAX ion-trap mass spectrometer, with an ESI ion source (Figures S16−S18).

PNA-1. MW: 3006.2 u.m.a.; UHPLC-MS (positive mode): 1003.08 $[PNA\text{-}1 + 3H]^{3+}$; 752.67 $[PNA\text{-}1 + 4H]^{4+}$; 602.33 $[PNA\text{-}1 + 5H]^{5+}$; 502.17 $[PNA\text{-}1 + 6H]^{6+}$; 430.50 $[PNA\text{-}1 + 7H]^{7+}$ m/z.

PNA-2. MW: 3031.2 u.m.a.; UHPLC-MS (positive mode): 1011.67 $[PNA\text{-}2 + 3H]^{3+}$; 758.83 $[PNA\text{-}2 + 4H]^{4+}$; 607.25 $[PNA\text{-}2 + 5H]^{5+}$; 506.33 $[PNA\text{-}2 + 6H]^{6+}$; 434.08 $[PNA\text{-}2 + 7H]^{7+}$ m/z.

PNA-Cum. MW: 3611.8 u.m.a.; UHPLC-MS (positive mode): 1204.58 $[PNA\text{-}Cum + 3H]^{3+}$; 903.95 $[PNA\text{-}Cum + 4H]^{4+}$; 723.33 $[PNA\text{-}Cum + 5H]^{5+}$; 602.92 $[PNA\text{-}Cum + 6H]^{6+}$; 517.00 $[PNA\text{-}Cum + 7H]^{7+}$ m/z.

Chemometric Analysis on CD Spectra. CD spectra were first explored by Principal Component Analysis (PCA), and consequently, Soft Independent Modeling of Class Analogy (SIMCA) was exploited as a class-modeling algorithm to model relevant G4 topologies and verify new samples' compatibility with them. For both PCA and SIMCA, the best results were obtained on centered CD spectra, without any further pre-treatment. Both the tools were first run on the reference data set found in the literature, made of 23 G4s CD spectra (7 parallels, 8 hybrids, and 8 antiparallels).[35] Subsequently, the data set was used for analyzing the contribution of G4-stabilizing ligands (HPHAM, PDS, Braco19) and PNA conjugates (PNA-1, PNA-2, PNA-Cum) on pApoE-G4s topologies. Chemometric calculations were performed using MatLab toolboxes developed by Ballabio and co-workers.[53,54]

■ ASSOCIATED CONTENT

Data Availability Statement

The data sets supporting the conclusions of this article are included within the article (and its Supporting Information). Additional material or information can be provided upon request by contacting the corresponding author.

Supporting Information

The Supporting Information is available free of charge at https://pubs.acs.org/doi/10.1021/acsomega.4c06430.

GC-Content distribution; putative G-quadruplex sequences identified in the ApoE promoter region; estimation of the fractions of tertiary and secondary structural elements of ApoE G4s; CD-melting data; UV-melting model-dependent thermodynamic parameters; TDS spectra; G4-ligands; CD spectra and estimated fractions of the tertiary structural elements of pApoE-G4s; PNA sequences; chemometric data; analytic HPLC profiles; DNA model oligonucleotides and primers used; UHPLC-MS data (PDF)

■ AUTHOR INFORMATION

Corresponding Author

Valentina Pirota − *Department of Chemistry, University of Pavia, I-27100 Pavia, Italy; G4-INTERACT, USERN, I-27100 Pavia, Italy;* orcid.org/0000-0002-6683-1726; Email: valentina.pirota@unipv.it

Authors

Angela Dello Stritto − *Istituto di Genetica Molecolare "Luigi Luca Cavalli-Sforza", I-27100 Pavia, Italy*

Lisa Rita Magnaghi − *Department of Chemistry, University of Pavia, I-27100 Pavia, Italy; Unità di Ricerca di Pavia, I-50121 Firenze, Italy;* orcid.org/0000-0002-4484-4788

Raffaela Biesuz − *Department of Chemistry, University of Pavia, I-27100 Pavia, Italy; Unità di Ricerca di Pavia, I-50121 Firenze, Italy*

Filippo Doria − *Department of Chemistry, University of Pavia, I-27100 Pavia, Italy;* orcid.org/0000-0002-1308-1060

Mariella Mella − *Department of Chemistry, University of Pavia, I-27100 Pavia, Italy*

Mauro Freccero − *Department of Chemistry, University of Pavia, I-27100 Pavia, Italy;* orcid.org/0000-0002-7438-1526

Emmanuele Crespan − *Istituto di Genetica Molecolare "Luigi Luca Cavalli-Sforza", I-27100 Pavia, Italy*

Complete contact information is available at: https://pubs.acs.org/10.1021/acsomega.4c06430

Author Contributions

V.P. and A.D.S. contributed equally to the experimental part of this work.

Funding

E.C. and A.D.S. were supported by the Italian Association for cancer Research AIRC [IG2020 no. 24448 to E.C.]

Notes

The authors declare no competing financial interest.

■ ACKNOWLEDGMENTS

The authors express their gratitude to Dr. Teresa Recca and the 'Centro Grandi Strumenti' at the University of Pavia for providing access to the Bruker Avance NEO 700 MHz spectrometer. They also extend their thanks to Prof. Paolo Oliveri, from Genoa University, for his support with the class-modeling data processing.

■ REFERENCES

(1) Ren, L.; Yi, J.; Li, W.; Zheng, X.; Liu, J.; Wang, J.; Du, G. Apolipoproteins and cancer. *Cancer medicine* **2019**, *8* (16), 7032−7043.

(2) Luo, J.; Song, J.; Feng, P.; Wang, Y.; Long, W.; Liu, M.; Li, L. Elevated serum apolipoprotein E is associated with metastasis and poor prognosis of non-small cell lung cancer. *Tumor Biology* **2016**, *37* (8), 10715−10721.

(3) Zhao, Z.; Zou, S.; Guan, X.; Wang, M.; Jiang, Z.; Liu, Z.; Li, C.; Lin, H.; Liu, X.; Yang, R.; et al. Apolipoprotein E Overexpression Is Associated With Tumor Progression and Poor Survival in Colorectal Cancer. *Front Genet* **2018**, *9*, 650.

(4) Lee, Y. S.; Yeo, I. J.; Kim, K. C.; Han, S.-B.; Hong, J. T. Inhibition of Lung Tumor Development in ApoE Knockout Mice via Enhancement of TREM-1 Dependent NK Cell Cytotoxicity. *Front. Immunol.* **2019**, *10*, 01379.

(5) Su, W. P.; Chen, Y. T.; Lai, W. W.; Lin, C. C.; Yan, J. J.; Su, W. C. Apolipoprotein E expression promotes lung adenocarcinoma proliferation and migration and as a potential survival marker in lung cancer. *Lung Cancer* **2011**, *71* (1), 28−33.

(6) Liu, M.; Feng, L.-X.; Sun, P.; Liu, W.; Mi, T.; Lei, M.; Wu, W.; Jiang, B.; Yang, M.; Hu, L.; et al. Knockdown of Apolipoprotein E Enhanced Sensitivity of Hep3B Cells to Cardiac Steroids via Regulating Na+/K+-ATPase Signalosome. *Molecular Cancer Therapeutics* **2016**, *15* (12), 2955−2965.

(7) Mahley, R. W. Central Nervous System Lipoproteins: ApoE and Regulation of Cholesterol Metabolism. *Arterioscler Thromb Vasc Biol.* **2016**, *36* (7), 1305−1315.

(8) Van Giau, V.; Bagyinszky, E.; An, S. S.; Kim, S. Role of apolipoprotein E in neurodegenerative diseases. *Neuropsychiatr. Dis. Treat.* **2015**, *11*, 1723−1737.
(9) Yamazaki, Y.; Zhao, N.; Caulfield, T. R.; Liu, C.-C.; Bu, G. Apolipoprotein E and Alzheimer disease: pathobiology and targeting strategies. *Nature Reviews Neurology* **2019**, *15* (9), 501−518.
(10) Kim, J.; Jiang, H.; Park, S.; Eltorai, A. E.; Stewart, F. R.; Yoon, H.; Basak, J. M.; Finn, M. B.; Holtzman, D. M. Haploinsufficiency of human APOE reduces amyloid deposition in a mouse model of amyloid-beta amyloidosis. *J. Neurosci.* **2011**, *31* (49), 18007−18012.
(11) Wisniewski, T.; Drummond, E. APOE-amyloid interaction: Therapeutic targets. *Neurobiol Dis* **2020**, *138*, 104784.
(12) Mak, A. C.; Pullinger, C. R.; Tang, L. F.; Wong, J. S.; Deo, R. C.; Schwarz, J. M.; Gugliucci, A.; Movsesyan, I.; Ishida, B. Y.; Chu, C.; et al. Effects of the absence of apolipoprotein e on lipoproteins, neurocognitive function, and retinal function. *JAMA Neurol* **2014**, *71* (10), 1228−1236.
(13) Kosiol, N.; Juranek, S.; Brossart, P.; Heine, A.; Paeschke, K. G-quadruplexes: a promising target for cancer therapy. *Molecular Cancer* **2021**, *20* (1), 40.
(14) Sato, K.; Knipscheer, P. G-quadruplex resolution: From molecular mechanisms to physiological relevance. *DNA Repair* **2023**, *130*, 103552.
(15) Dell'Oca, M. C.; Quadri, R.; Bernini, G. M.; Menin, L.; Grasso, L.; Rondelli, D.; Yazici, O.; Sertic, S.; Marini, F.; Pellicioli, A. Spotlight on G-Quadruplexes: From Structure and Modulation to Physiological and Pathological Roles. *Int. J. Mol. Sci.* **2024**, *25*, 3162.
(16) Varshney, D.; Spiegel, J.; Zyner, K.; Tannahill, D.; Balasubramanian, S. The regulation and functions of DNA and RNA G-quadruplexes. *Nat. Rev. Mol. Cell Biol.* **2020**, *21* (8), 459−474.
(17) Spiegel, J.; Adhikari, S.; Balasubramanian, S. The Structure and Function of DNA G-Quadruplexes. *Trends Chem.* **2020**, *2* (2), 123−136.
(18) Di Antonio, M.; Ponjavic, A.; Radzevičius, A.; Ranasinghe, R. T.; Catalano, M.; Zhang, X.; Shen, J.; Needham, L.-M.; Lee, S. F.; Klenerman, D.; et al. Single-molecule visualization of DNA G-quadruplex formation in live cells. *Nat. Chem.* **2020**, *12* (9), 832−837.
(19) Pirota, V.; Rey, F.; Esposito, L.; Fantini, V.; Pandini, C.; Maghraby, E.; Di Gerlando, R.; Doria, F.; Mella, M.; Pansarasa, O.; et al. Effective lowering of α-synuclein expression by targeting G-quadruplex structures within the SNCA gene. *Int. J. Biol. Macromol.* **2024**, *277*, 134417.
(20) Kharel, P.; Becker, G.; Tsvetkov, V.; Ivanov, P. Properties and biological impact of RNA G-quadruplexes: from order to turmoil and back. *Nucleic Acids Res.* **2020**, *48* (22), 12534−12555.
(21) Largy, E.; Mergny, J. L.; Gabelica, V. Role of Alkali Metal Ions in G-Quadruplex Nucleic Acid Structure and Stability. *Met Ions Life Sci.* **2016**, *16*, 203−258.
(22) Balasubramanian, S.; Hurley, L. H.; Neidle, S. Targeting G-quadruplexes in gene promoters: a novel anticancer strategy? *Nat. Rev. Drug Discov* **2011**, *10* (4), 261−275.
(23) Cebrián, R.; Belmonte-Reche, E.; Pirota, V.; de Jong, A.; Morales, J. C.; Freccero, M.; Doria, F.; Kuipers, O. P. G-Quadruplex DNA as a Target in Pathogenic Bacteria: Efficacy of an Extended Naphthalene Diimide Ligand and Its Mode of Action. *J. Med. Chem.* **2022**, *65*, 4752.
(24) Burger, A. M.; Dai, F.; Schultes, C. M.; Reszka, A. P.; Moore, M. J.; Double, J. A.; Neidle, S. The G-quadruplex-interactive molecule BRACO-19 inhibits tumor growth, consistent with telomere targeting and interference with telomerase function. *Cancer Res.* **2005**, *65* (4), 1489−1496.
(25) Hou, Y.; Gan, T.; Fang, T.; Zhao, Y.; Luo, Q.; Liu, X.; Qi, L.; Zhang, Y.; Jia, F.; Han, J.; et al. G-quadruplex inducer/stabilizer pyridostatin targets SUB1 to promote cytotoxicity of a transplatinum complex. *Nucleic Acids Res.* **2022**, *50* (6), 3070−3082.
(26) Green, J. J.; Ying, L.; Klenerman, D.; Balasubramanian, S. Kinetics of Unfolding the Human Telomeric DNA Quadruplex Using a PNA Trap. *J. Am. Chem. Soc.* **2003**, *125* (13), 3763−3767.
(27) Robinson, J.; Raguseo, F.; Nuccio, S. P.; Liano, D.; Di Antonio, M. DNA G-quadruplex structures: more than simple roadblocks to transcription? *Nucleic Acids Res.* **2021**, *49* (15), 8419−8431.
(28) Fracchioni, G.; Vailati, S.; Grazioli, M.; Pirota, V. Structural Unfolding of G-Quadruplexes: From Small Molecules to Antisense Strategies. *Molecules* **2024**, *29*, 3488.
(29) Kikin, O.; D'Antonio, L.; Bagga, P. S. QGRS Mapper: a web-based server for predicting G-quadruplexes in nucleotide sequences. *Nucleic Acids Res.* **2006**, *34*, W676−W682.
(30) Bedrat, A.; Lacroix, L.; Mergny, J. L. Re-evaluation of G-quadruplex propensity with G4Hunter. *Nucleic Acids Res.* **2016**, *44* (4), 1746−1759.
(31) Patel, D. J.; Phan, A. T.; Kuryavyi, V. Human telomere, oncogenic promoter and 5′-UTR G-quadruplexes: diverse higher order DNA and RNA targets for cancer therapeutics. *Nucleic Acids Res.* **2007**, *35* (22), 7429−7455.
(32) Lago, S.; Cernilogar, F. M.; Kazerani, M.; Moreno, H. D.; Nadai, M.; Schotta, G.; Richter, S. N. Promoter G-quadruplexes and transcription factors cooperate to shape the cell type-specific transcriptome*bioRxiv*, August 27, 2020, 2020.2008.2027.236778. DOI: 10.1101/2020.08.27.236778
(33) Kardassis, D.; Gafencu, A.; Zannis, V. I.; Davalos, A. Regulation of HDL genes: transcriptional, posttranscriptional, and posttranslational. *Handb Exp Pharmacol* **2015**, *224*, 113−179.
(34) Gafencu, A. V.; Robciuc, M. R.; Fuior, E.; Zannis, V. I.; Kardassis, D.; Simionescu, M. Inflammatory signaling pathways regulating ApoE gene expression in macrophages. *J. Biol. Chem.* **2007**, *282* (30), 21776−21785.
(35) Del Villar-Guerra, R.; Trent, J. O.; Chaires, J. B. G-Quadruplex Secondary Structure Obtained from Circular Dichroism Spectroscopy. *Angew. Chem., Int. Ed. Engl.* **2018**, *57* (24), 7171−7175.
(36) Vorlíčková, M.; Kejnovská, I.; Bednářová, K.; Renčiuk, D.; Kypr, J. Circular Dichroism Spectroscopy of DNA: From Duplexes to Quadruplexes. *Chirality* **2012**, *24* (9), 691−698.
(37) Del Villar-Guerra, R.; Gray, R. D.; Chaires, J. B. Characterization of Quadruplex DNA Structure by Circular Dichroism. *Curr. Protoc. Nucleic Acid Chem.* **2017**, *68*, 17.18.11−17.18.16.
(38) Lin, C.; Dickerhoff, J.; Yang, D. NMR Studies of G-Quadruplex Structures and G-Quadruplex-Interactive Compounds. *Methods Mol. Biol.* **2019**, *2035*, 157−176.
(39) Nadai, M.; Doria, F.; Scalabrin, M.; Pirota, V.; Grande, V.; Bergamaschi, G.; Amendola, V.; Winnerdy, F. R.; Phan, A. T.; Richter, S. N.; et al. A Catalytic and Selective Scissoring Molecular Tool for Quadruplex Nucleic Acids. *J. Am. Chem. Soc.* **2018**, *140* (44), 14528−14532.
(40) Mergny, J. L.; Lacroix, L. UV Melting of G-Quadruplexes. *Curr. Protoc. Nucleic Acid Chem.* **2009**, 17.1.1−17.1.15.
(41) Karsisiotis, A. I.; Hessari, N. M. a.; Novellino, E.; Spada, G. P.; Randazzo, A.; Webba da Silva, M. Topological Characterization of Nucleic Acid G-Quadruplexes by UV Absorption and Circular Dichroism. *Angew. Chem., Int. Ed.* **2011**, *50* (45), 10645−10648.
(42) Jamroskovic, J.; Obi, I.; Movahedi, A.; Chand, K.; Chorell, E.; Sabouri, N. Identification of putative G-quadruplex DNA structures in S. pombe genome by quantitative PCR stop assay. *DNA Repair* **2019**, *82*, 102678.
(43) Swenson, C. S.; Lackey, H. H.; Reece, E. J.; Harris, J. M.; Heemstra, J. M.; Peterson, E. M. Evaluating the effect of ionic strength on PNA:DNA duplex formation kinetics. *RSC Chemical Biology* **2021**, *2* (4), 1249−1256.
(44) Tassinari, M.; Zuffo, M.; Nadai, M.; Pirota, V.; Sevilla Montalvo, A. C.; Doria, F.; Freccero, M.; Richter, S. N. Selective targeting of mutually exclusive DNA G-quadruplexes: HIV-1 LTR as paradigmatic model. *Nucleic Acids Res.* **2020**, *48* (9), 4627−4642.
(45) Sathyaseelan, C.; Vijayakumar, V.; Rathinavelan, T. CD-NuSS: A Web Server for the Automated Secondary Structural Characterization of the Nucleic Acids from Circular Dichroism Spectra Using Extreme Gradient Boosting Decision-Tree, Neural Network and Kohonen Algorithms. *J. Mol. Biol.* **2021**, *433* (11), 166629.

https://doi.org/10.1021/acsomega.4c06430
ACS Omega 2024, 9, 45203−45213

(46) Zimmer, D. P.; Crothers, D. M. NMR of enzymatically synthesized uniformly 13C15N-labeled DNA oligonucleotides. *Proc. Natl. Acad. Sci. U. S. A.* **1995**, *92* (8), 3091−3095.
(47) Oliveri, P.; Malegori, C.; Casale, M. Chemometrics and Statistics | Multivariate Classification Techniques. In *Encyclopedia of Analytical Science*, 3rd ed.; Worsfold, P., Poole, C., Townshend, A., Miró, M., Eds.; Academic Press, 2019; pp 481−486.
(48) Oliveri, P. Class-modelling in food analytical chemistry: Development, sampling, optimization and validation issues - A tutorial. *Anal. Chim. Acta* **2017**, *982*, 9−19.
(49) Doria, F.; Nadai, M.; Sattin, G.; Pasotti, L.; Richter, S. N.; Freccero, M. Water soluble extended naphthalene diimides as pH fluorescent sensors and G-quadruplex ligands. *Organic & Biomolecular Chemistry* **2012**, *10* (19), 3830−3840.
(50) Rodriguez, R.; Miller, K. M.; Forment, J. V.; Bradshaw, C. R.; Nikan, M.; Britton, S.; Oelschlaegel, T.; Xhemalce, B.; Balasubramanian, S.; Jackson, S. P. Small-molecule-induced DNA damage identifies alternative DNA structures in human genes. *Nat. Chem. Biol.* **2012**, *8* (3), 301−310.
(51) Carey, T. E.; Takahashi, T.; Resnick, L. A.; Oettgen, H. F.; Old, L. J. Cell surface antigens of human malignant melanoma: mixed hemadsorption assays for humoral immunity to cultured autologous melanoma cells. *Proc. Natl. Acad. Sci. U. S. A.* **1976**, *73* (9), 3278−3282.
(52) Liu, S.; Wang, W.-H.; Dang, Y.-L.; Fu, Y.; Sang, R. Rational design and efficient synthesis of a fluorescent-labeled jasmonate. *Tetrahedron Lett.* **2012**, *53* (32), 4235−4239.
(53) Ballabio, D.; Consonni, V. Classification tools in chemistry. Part 1: linear models. PLS-DA. *Analytical Methods* **2013**, *5* (16), 3790−3798.
(54) Ballabio, D. A MATLAB toolbox for Principal Component Analysis and unsupervised exploration of data structure. *Chemometrics and Intelligent Laboratory Systems* **2015**, *149*, 1−9.

https://doi.org/10.1021/acsomega.4c06430
ACS Omega 2024, 9, 45203−45213